Refractory High-Entropy Alloys Produced from Elemental Powders by Severe Plastic Deformation

Rimma Lapovok, Mahmoud Reza Ghandehari Ferdowsi, Vadim Shterner, Peter D. Hodgson, Andrey Mazilkin, Evgeniy Boltynjuk, Roman Kulagin, and Sheldon Lee Semiatin*

A comparative investigation of two fundamentally different approaches for the synthesis, microstructure evolution, and mechanical properties of the refractory high-entropy alloys (RHEA) HfNbTaTiZr and HfNbTiZr is performed. The two methods comprises conventional arc (button) melting and a powder route based on mechanical alloying and consolidation via severe plastic deformation. In particular, blended elemental powder is pre-compacted and subjected to one or four passes of equal channel angular pressing (ECAP) at 500 °C and then 10 revolutions of high pressure torsion (HPT) at room temperature to an effective strain between 4 and 40. Some samples are then annealed at 500 °C for 1 h to investigate the thermal stability of the phases. The four ECAP passes at 500 °C do not result in the formation of the body-centered cubic (BCC) phase typical for the program RHEAs despite the presence of interfacial zones between particles and defect-driven diffusion. Nevertheless, a single ECAP pass is sufficient to create a solid bulk sample for subsequent HPT. After 10 HPT revolutions, in contrast to melting route resulting in a single BCC phase alloy, both alloys form new phases comprising a Nb-rich BCC phase and a ZrHf-rich HCP phase in both alloys.

1. Introduction

High entropy alloys (HEAs) have stimulated a new era in alloy development. They rely on the manipulation of composition, often incorporating a variety of phases to enhance the properties.

R. Lapovok, M. R. G. Ferdowsi, V. Shterner, P. D. Hodgson
Institute for Frontier Materials
Deakin University
Waurn Ponds, VIC 3216, Australia
E-mail: r.lapovok@deakin.edu.au

A. Mazilkin, E. Boltynjuk, R. Kulagin
Institute of Nanotechnology
Karlsruhe Institute of Technology
76344 Eggenstein-Leopoldshafen, Germany

S. L. Semiatin
MRL Materials Resources LLC
Xenia Township, OH 45385, USA

Typically, HEAs are synthesized by a melting route; however, such an approach poses significant challenges in controlling chemical homogeneity and the size and distribution of the phases.[1] This manufacturing technology is an energy-consuming process and is not environmentally friendly. The complex composition of refractory-high-entropy alloys (RHEAs) with a wide variety of melting temperatures for the constituent elements from 1660 °C (Ti) to 2996 °C (Ta) leads to chemical segregation and a dendritic microstructure with a non-uniform distribution of elements, e.g., Nb and Ti are mainly segregated to the dendrites.[2] Several techniques have been developed to reduce this chemical inhomogeneity, such as an increase in the cooling rate and/or a prolonged heat treatment at a high temperature, which can be quite costly.

Elemental interactions are much more readily controlled if they occur in the solid state by techniques such as mechanical alloying. Mechanical alloying, which is typically carried out at low homologous temperatures (0.3–0.4 T_m), avoids the problems of melting/casting methods such as chemical segregation and is applicable to components with very different melting temperatures. Moreover, mechanical alloying can be used to synthesize alloys with novel phases which cannot be obtained by melting routes.[3,4]

It has been demonstrated previously that the production of solid billets through severe-plastic-deformation (SPD) methods using powders[5] is beneficial for alloy design, enabling the attainment of properties that are not possible in cast billets of the same nominal composition.[6,7] Specifically, SPD of powders relies on attrition/inter-particle mechanical alloying and the enhancement of diffusion associated with dislocation-substructure formation and grain refinement within deformed powder particles. The resulting microstructure tends to contain both high-angle and low-angle grain boundaries which can play an important role in the overall rate of diffusional intermixing, in spite of the relatively low diffusivities in refractory metals in general and RHEAs in particular. Smaller grain size increases the number of short-circuit paths for mass transport via grain-boundary diffusion. Moreover, it has been shown that highly-defective, ultrafine-grain microstructures substantially accelerate self-diffusion,[8] and thus promote diffusion bonding, inter-alloying, and the formation of new phases.

The combination of mechanical alloying and consolidation of powders via SPD processing may be expected to result in new nano-scale structures and phases with enhanced mechanical properties. Prior work has focused primarily on melting followed by SPD for RHEAs such as HfNbTaTiZr[9–11] and HfNbTiZr.[12–14] The alloys were typically produced via vacuum arc (button) melting followed by annealing and rolling or other thermomechanical treatments. For instance, the research presented in refs. [9,10] examined the properties and structure of HfNbTaTiZr after room temperature rolling to a true strain of ≈2. These studies[9–14] provided a solid foundation for comparison to the same/similar alloys produced via arc melting and plastic deformation.

It is important to note that while SPD techniques have been applied to HEAs synthesized via melting, only a few papers have explored the possibility of producing HEAs using the powder route,[15–17] which is the focus of the present article. The systems investigated were not relevant RHEAs, e.g., the CoCrFeMnNi ('Cantor') alloy was produced via high-pressure torsion (HPT) and reported in ref. [18]. Typically, these prior studies involved high-pressure and high-temperature sintering methods, which differ from the low-temperature methods described in the present work.

To the best of our knowledge, there has been no other research on the manufacturing of RHAEs through the solid-state joining of elemental powders at low temperatures. Despite ongoing research related to equiatomic RHEAs, refractory complex concentrated alloys (RCCAs)[19,20] may provide opportunities to create single- and multi- phase materials with better properties. Nevertheless, the majority of the published literature for the materials studied herein, i.e., the equiatomic HfNbTaTiZr and HfNbTiZr systems, has suggested that a single body-centered cubic (BCC) phase is developed when the material is synthesized by arc melting. Investigating the phases formed as a result of the warm SPD process is a crucial fundamental objective of this research. In essence, the current approach facilitated the exploration of mechanisms involved in the formation of new phases and enabled variations in composition and thereby the optimization of RHEAs.

2. Experimental Section

2.1. Powder Consolidation via Severe Plastic Deformation

Two RHEA compositions, HfNbTaTiZr and HfNbTiZr, were made from blended-elemental (BE) powders (mesh 325). The powders were handled in a Vigor argon-filled glove box with an oxygen level <0.002 ppm and a moisture level <0.1 ppm. The blends were made with calculated weight fractions to create M1 ($Hf_{20}Nb_{20}Ta_{20}Ti_{20}Zr_{20}$) and M2 ($Hf_{25}Nb_{25}Ti_{25}Zr_{25}$) equiatomic mixtures. These powder mixtures were consolidated via two different SPD routes: 1) four passes (route B_C) of equal channel angular extrusion (ECAP) at 50 °C and 2) one pass of ECAP at 50 °C followed by ten revolutions of HPT at room temperature. To investigate the thermal stability of the discovered phases, some of these deformed samples were annealed at 500 °C for 1 h in a vacuum furnace (designated hereafter as "An" samples).

The hydrostatic pressure applied during ECAP was 250 MPa, while for HPT it was 5 GPa. To perform ECAP at high temperature without oxygen ingress, square copper cans with tight lids were used (**Figure 1**a). These cans were filled with the powder mixture, pre-compacted manually by rod, and then sealed with a tight-fit-lid in the glove box. Following preheating, each sample was inserted into a 90° ECAP die with a square cross-section. A sample pressed in such a die keeps its dimensions through all four passes (Figure 1b). After one ECAP pass, some samples were sliced into plates ≈2 mm thick and then subjected to HPT. During HPT, the peripheral copper-can separated from the RHEA sample due to the high friction forces, resulting in a circular disc between the anvils (Figure 1c). The sample nomenclature and processing conditions for the experiments are given in **Table 1**, in which ε is the accumulated effective strain, σ is the hydrostatic pressure, and T is the processing temperature.

2.2. Mechanical-Property Testing

After ECAP, each sample was removed from its copper can, and lathe turned to produce cylindrical samples with diameter of 6.30 ± 0.25 mm and height of 9.60 ± 0.43 mm. Compression testing was then conducted at room temperature using an Instron 5967 universal testing machine equipped with a 30 kN load cell. Deformation was performed under constant-crosshead-speed conditions with an initial strain rate of 5×10^{-4} s^{-1}. Yield stress (σ_y), ultimate tensile stress (σ_u), and ductility (δ) were obtained.

The Vickers microhardness for all samples after various treatments was determined using Buehler Micromet 5104. All measurements were carried out at a load of 0.5 N and holding time of 10 s. The measurements were done in triplicate along three different diameters of the round samples; the standard deviation from the average was 7.2%.

2.3. Microstructure Characterization

The microstructure of samples produced by different routes was characterized using a JEOL 7800 FEG scanning electron microscope (SEM) equipped with an energy-dispersive X-ray spectroscopy (EDS) detector; using an accelerating voltage of 20 kV and working distance of ≈10 mm. Images were taken using a lower electron detector (LED) equivalent to SE2 detector. Prior to examination, samples were mechanically ground using silicon carbide papers to 1200 grit after which they were polished with various abrasive suspension liquids to OP-S (0.05 μm).

The microstructures of the samples were also characterized using a JEOL 2100 F FEG TEM equipped with an EDS detector. For this purpose, samples were ground mechanically to ≈100 μm thickness. Then, a 3 mm disk was punched from the sample and its thickness was further reduced in the center to ≈20 μm with a Gatan dimple grinder. Finally, a Leica EM RES 102 ion mill was utilized at 5 kV and 2.2 mA to perforate the disk. Bright field images and diffraction patterns were captured at 200 kV. Elemental (composition) maps were also captured in the STEM mode using EDS.

2.4. Phase Determination

The phases present in the samples were identified by an X-ray diffraction (XRD) technique. A PANalytical X'Pert Pro MRD with Cu K$_\alpha$ radiation ($\lambda = 1.5406$ Å) and a 2×2 mm aperture size was used at 40 kV and 30 mA. The diffraction profiles were captured within

ADVANCED
SCIENCE NEWS
www.advancedsciencenews.com

ADVANCED
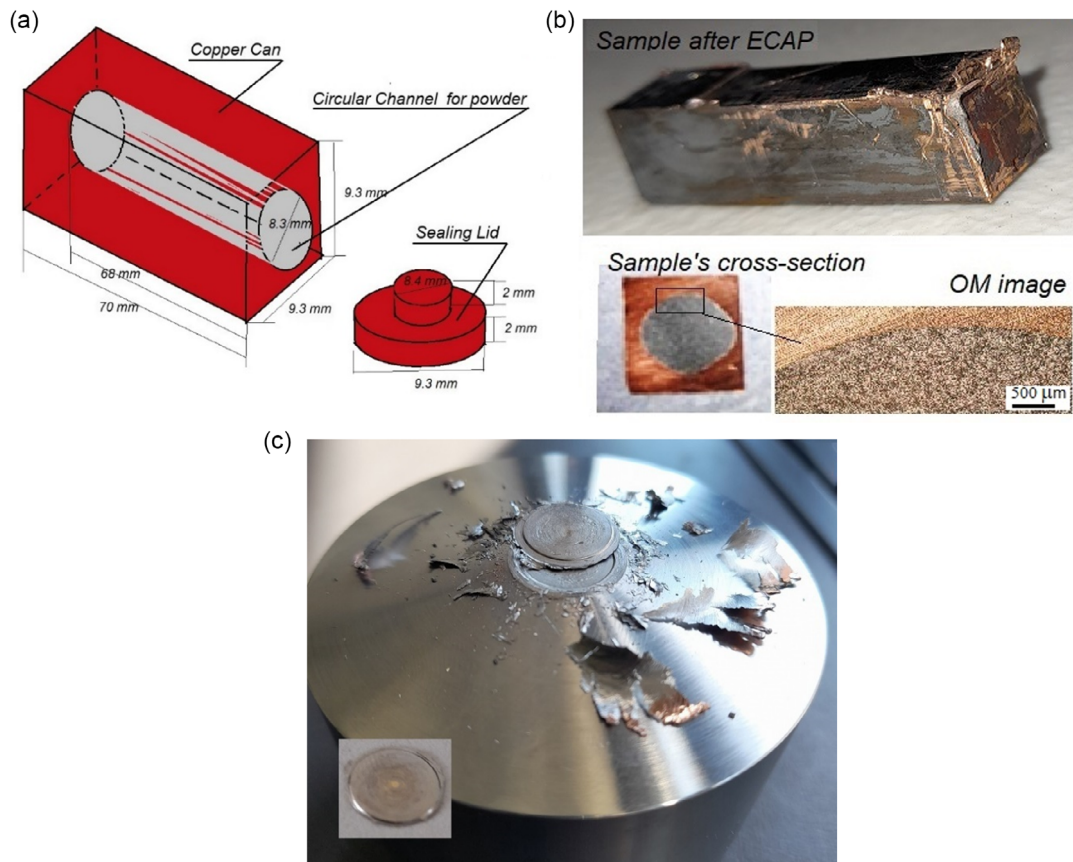ENGINEERING
MATERIALS
www.aem-journal.com

Figure 1. ECAP and HPT processing of powder mixtures: a) Copper can with lid; b) sample after ECAP with cross-section view after one ECAP pass and optical-microscopy image; and c) slice of sample subjected to one ECAP pass and HPT.

Table 1. Sample nomenclature and processing conditions ("*An*"-designates annealing).

BE-powder mixture	ECAP−4 passes	ECAP−1 pass + HPT (10 rev.)
	$T = 500\,°C$, $\varepsilon = 4.46$, $\sigma = 250$ MPa	$T = 500\,°C$, $\varepsilon = 1.15$, $\sigma = 250$ MPa; $T = 20\,°C$, $\varepsilon = 150$, $\sigma = 5$ GPa
HfNbTaTiZr	M1−ECAP4	M1−ECAP1−HPT
HfNbTiZr	M2−ECAP4	M2−ECAP1−HPT
HfNbTaTiZr	M1−ECAP4−An	M1−ECAP1−HPT−An
HfNbTiZr	M2−ECAP4−An	M2−ECAP1−HPT−An

2θ interval (30°…110°) with a step size of 0.02° and step time of 10 s. The acquired profiles were analyzed using the High-Score Plus software combined with the ICCD-PDF 4 2019 database.

3. Results and Discussion

Three physical mechanisms came into play at the interface between particles when they underwent severe plastic deformation with superimposed hydrostatic pressure, i.e., deformation-induced atomic intermixing, enhanced (pipe) diffusion caused by defects generated during severe plastic deformation, and the (potential) formation of new phases. All three mechanisms were observed to be active to some extent in the present work.

3.1. Deformation-Induced Atom Intermixing

Analysis of the microstructure of samples after one ECAP pass (M1-ECAP1 and M2-ECAP1) (**Figure 2**) confirmed previous findings for conventional alloys[6,7,21,22] that severe shear deformation, combined with imposed hydrostatic pressure, plays a crucial role in consolidating elemental powders. For the present RHEAs, excellent shape accommodation and bonding between particles was achieved. Such shape accommodation occurred through localized strain at the contact surfaces between particles with different hardness. Asperities on the harder particles act as rigid tools, penetrating the soft material, while the softer particles fill the valleys between asperities. This results in a nearly laminar flow pattern parallel to the shear plane of ECAP. Unlike ECAP deformation, the intermixing of multiple solids using HPT[18,23] clearly shows a turbulent flow pattern with vortices.

The present results also indicated that a single ECAP pass was sufficient to achieve high-density compacts of BE powders with very good mechanical properties, namely, strength ranging (700–900 MPa) and ductility ranging (0.7–1.0%), even at
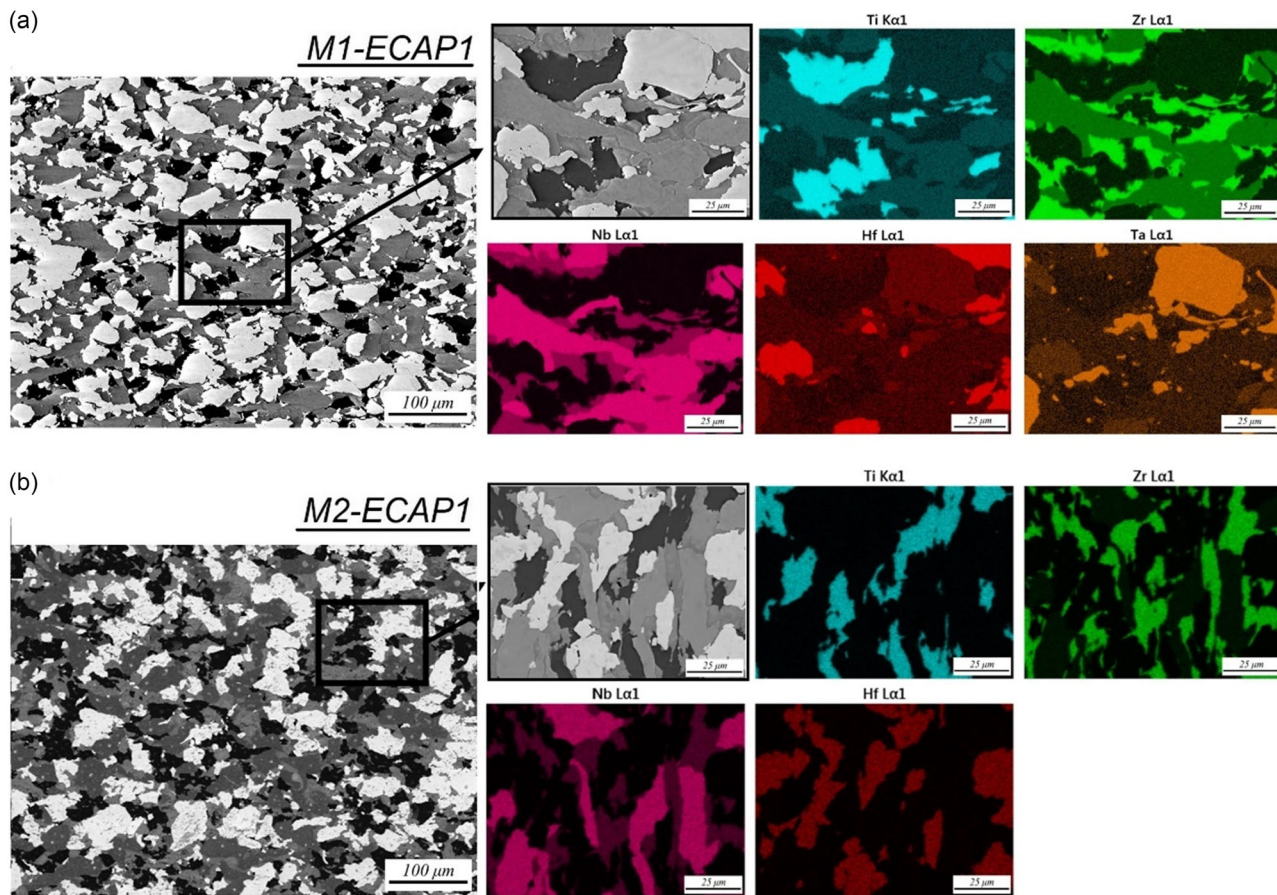
**ADVANCED
SCIENCE NEWS**

www.advancedsciencenews.com

**ADVANCED
ENGINEERING
MATERIALS**

www.aem-journal.com

Figure 2. SEM images of microstructure and elemental maps in samples: a) M1-ECAP1 and b) M2-ECAP1.

relatively low temperatures (**Figure 3**a). After four ECAP passes (effective strain ≈4.6), both materials exhibited a refined microstructure and strain hardening response in compression (Figure 3a), as will be discussed in Section 3.2. The strength and ductility of compacts also improved slightly for the samples, processed by four ECAP passes, which were heated and soaked for 5 min before each ECAP pass (**Table 2**). It should be noted that strength and ductility of obtained compacts cannot be compared to published mechanical properties of the targeted RHEAs because the phases, and therefore HEAs, have not been formed as results of ECAP. That will also be discussed further in Section 3.2. Only after HPT the phases typical for M1 and M2 RHEAs formed, which justifies the characterization of mechanical properties by Vickers hardness measurements due to small diameter of samples.

The Vickers microhardness measurements (Figure 3b) demonstrated an increase in strength with the accumulation of effective strain above 40 and its saturation in the outer region of the sample (about $r > 0.3 R$) These results are consistent with the published data for similar alloys synthesized by arc melting followed either by rolling or SPD, or by powder consolidation based on sintering and SPD.[9,12,13,15,16,24] Hardness range (Hv 500–550) for M1-ECAP1-HPT and M1-ECAP1-HPT exceeds the values published in these references. For example, in ref. [12],

Vickers hardness values after severe rolling of M2 samples produced by arc-melting and severe rolling are around Hv 310. Similarly, in ref. [9], the M1 samples produced by arc-melting and severe rolling are around (Hv 380). The arc melted M2 samples subjected to HPT, presented in ref. [13], showed better hardness values around (Hv 440).

After short annealing the Vickers hardness increased significantly for all samples deformed by four passes of ECAP and all samples deformed by one ECAP pass followed by HPT, Figure 3c,d, to the range of Hv 650–800. For example, compare to results presented in ref. [12], hardness after low temperature annealing (450 °C) increased only by 30 and then dropped with increasing annealing temperature. The increase of harness by Hv 150–200 is presumably associated with transformation of BCC phase into new phases as will be discussed in Section 3.4. Similar increase in hardness due to formation of a new FCC phase is discussed in ref. [17]. Other factors that could explain the increase in hardness after short low-temperature annealing in severely deformed pure metals[25–27] cannot be excluded. Since the hardening attributed to segregated impurities at grain boundaries is not applicable in our case of high-purity metals, the increase in hardness could be attributed to either phase transformation or the agglomeration and annihilation of deformation-induced vacancies (as discussed in ref. [26]).
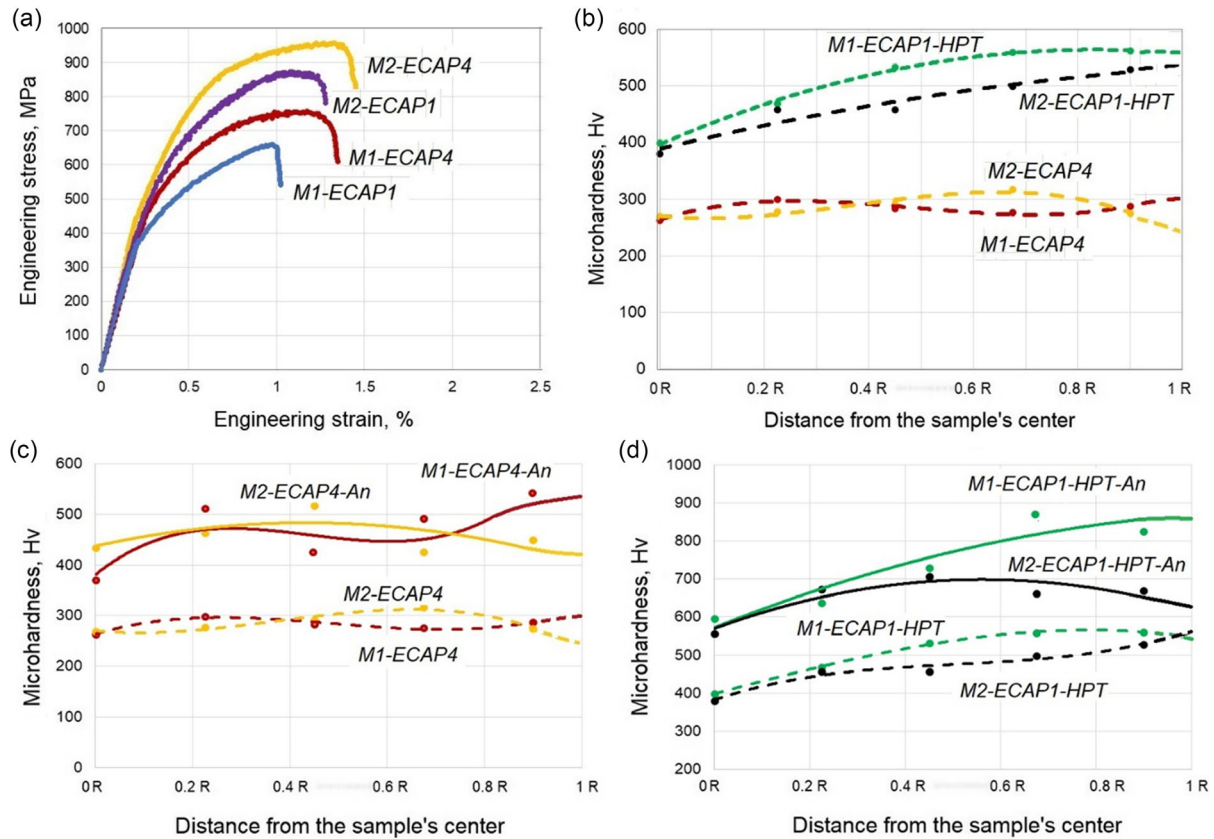
Figure 3. Mechanical properties: a) Engineering stress versus engineering strain in compression for M1 and M2 samples after one and four ECAP passes; and Vickers microhardness along the sample radius for b) M1 and M2 samples after ECAP4 and ECAP1 + HPT; c) M1 and M2 samples in deformed (ECAP4) and annealed conditions; d) M1 and M2 samples in deformed (ECAP1 + HPT) and annealed conditions.

Table 2. Mechanical properties of compacts after one and four ECAP passes.

	σ_y [MPa]	σ_u [MPa]	δ [%]	–	σ_y [MPa]	σ_u [MPa]	δ [%]
M1-ECAP1	410	661	0.82	M1-ECAP4	504	758	1.15
M2-ECAP1	481	874	1.08	M2-ECAP4	564	958	1.26

SEM images of the microstructure after a single ECAP pass (Figure 2) also revealed a relative lack of both a significant disturbance in particle shape and turbulent flow during intermixing. Although the application of an effective strain of 1.15 during one ECAP pass was close to the effective threshold strain of 1.20 required for the occurrence of mechanical intermixing and the start of chaotic mass transfer during deformation in shear,[23] such phenomena were not observed in the present work even after the second and third ECAP passes (effective strain = 2.3 and 3.45, respectively). Only when the number of passes was increased to four (M1-ECAP4 and M2-ECAP4), corresponding to a strain of 4.6, did the flow pattern and intermixing become more pronounced (**Figure 4**). This phenomenon can be attributed to the difference between stirring fully dense solids and particulate

metals, the latter exhibiting significantly lower resistance to turbulent flow than the former.

Microstructures like those in M1-ECAP4 and M2-ECAP4 were observed in the central region of samples M1–ECAP1–HPT and M2–ECAP1–HPT, indicating that the accumulated plastic strain here was close to 4.6. Thus, the deformation during HPT was not distributed uniformly along the radius of the disc. In particular, according to an analytical model presented in ref. [28], the shear strain level is lower in the central region lying between $R = 0$ and approximately one-third of the radius (0.3 R), compared to that developed in the middle and outer edge of the specimen at the beginning of the HPT. The extent of this low-deformation region gradually diminishes as the number of revolutions increases. However, even after ten revolutions, the central regions of the samples investigated here did not achieve uniformity. The images in **Figure 5** depict the microstructures of M1-ECAP1 and M2-ECAP1 along the radius after ten HPT revolutions. Similar images were observed after five HPT revolutions. Overall, the images demonstrated excellent intermixing for only the outer two-thirds of the radius in the samples.

Within the central region of samples M1-ECAP1-HPT and M2-ECAP1-HPT ($r < 0.3 R$) and for samples M1-ECAP4 and M2-ECAP4, for which the accumulated strain was 4.6, a
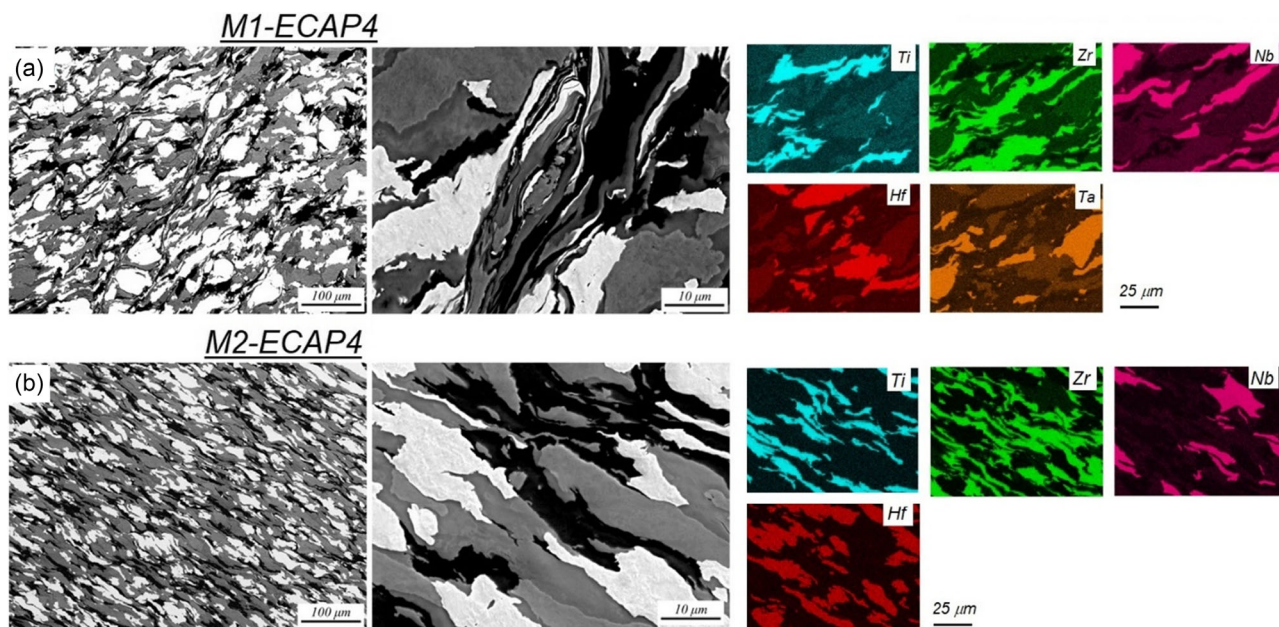
2301949 (5 of 15)

**ADVANCED
SCIENCE NEWS**

www.advancedsciencenews.com

**ADVANCED
ENGINEERING
MATERIALS**

www.aem-journal.com

Figure 4. SEM images of microstructure and elemental maps in samples a) M1-ECAP4; and b) M2-ECAP4.
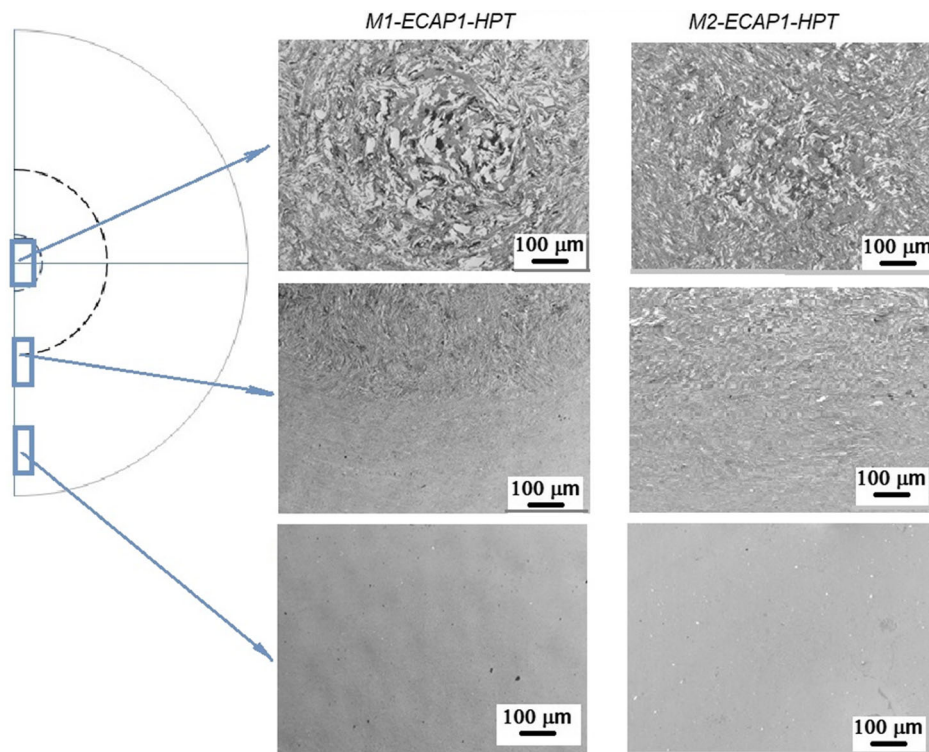

Figure 5. SEM images of microstructure in samples M1-ECAP4 and M2-ECAP4 after ten revolutions of HPT showing the saturation of intermixing and grain refinement within the outer two-thirds of the radius.

turbulent flow pattern and partial atomic intermixing were observed (Figure 4 and 5).

Except for a few unmixed particles, the images in **Figure 6** showed nearly equiatomic mixtures in the outer region

($r > 0.3 R$) of samples M1-ECAP1-HPT and M2-ECAP1-HPT. The accumulated plastic strain in this region exceeded the theoretically predicted level of 40.[28] However, slippage along the tooling contact surfaces may have reduced the local accumulated
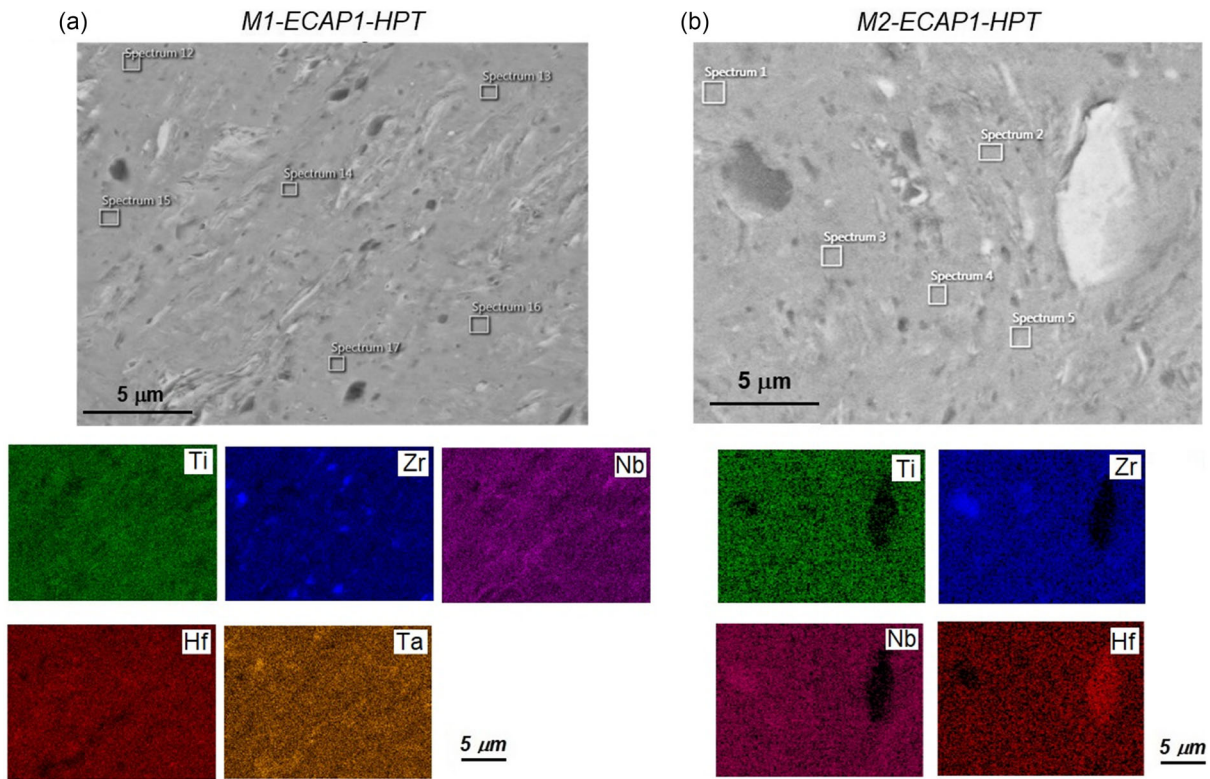
Figure 6. SEM images indicating the locations at which EDS spectra were collected (boxes) and elemental maps in outer region ($r > 0.3$ R) for samples: a) M1-ECAP1-HPT; and b) M2-ECAP1-HPT.

strain here. The EDS-measured compositions (**Table 3**) revealed some small deviations from the theoretical equiatomic values of 20 at% for M1 and 25 at% for M2 on this scale.

3.2. Formation of Ultrafine Grain Structure Promoting Defect-Driven Diffusion

Figure 7 shows STEM BF images of M1 and M2 samples after four ECAP passes. In these images the phases were identified by EDS elemental analysis; they are marked correspondingly in the images. It can be seen that an ultrafine grain structure with sharp, high-angle boundaries was obtained after four ECAP passes for both M1 and M2. The degree of grain refinement within each elemental powder particle depended not only on the average local level of accumulated strain but also on the specific particle element. Thus, the grain size in different particles varied between ≈200 and 800 nm as shown in Figure 7c,d.

The potential for defect-driven diffusion during severe deformation at 500 °C was elucidated in multiple-line-scan elemental-profile analyses using a beam size of 1.5 nm and comprising >130 lines across several contact planes between elemental powder particles for both M1 and M2. Examples of the elemental profiles for M1-ECAP4 and M2-ECAP4 are shown in **Figure 8**. The diffusion distance was estimated from the length of the profile segments for which a visible change in concentration was observed. The resulting average diffusion distances (**Table 4**) exhibited very large values of standard deviation, suggesting that the

Table 3. Composition in the selected locations of the samples based on the EDS measurements (Figure 6).

Spectrum number (Figure 6)	M1-ECAP1-HPT				
	Hf [at%]	Nb [at%]	Ti [at%]	Zr [at%]	Ta [at%]
12	20	20	21.	18	21
13	20	19	22	19	20
14	21	22	20	18	19
15	20	20	20	19	20
16	23	17	22	18	20
17	20	19	21	19	21
	M1-ECAP1-HPT				
1	25	28	27	20	–
2	27	22	28	23	–
3	22	32	24	22	–
4	25	25	27	23	–
5	28	24	26	22	–

measurements depended on the inclination of the grain boundary with respect to the electron beam, i.e., a stereological effect.

Based on literature data,[29] the present results suggested the formation of binary phases in M1-ECAP4 and M2-ECAP4 due to diffusion, a behavior which will be further discussed in Section 3.3.
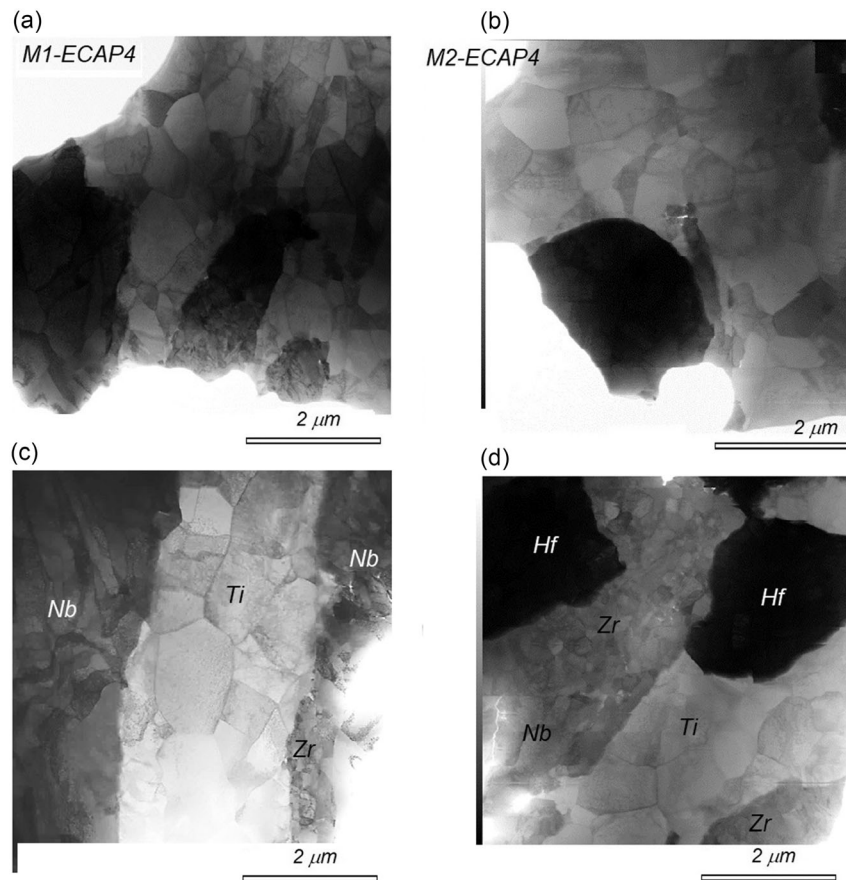
**ADVANCED
SCIENCE NEWS**

www.advancedsciencenews.com

**ADVANCED
ENGINEERING
MATERIALS**

www.aem-journal.com

Figure 7. Bright-field STEM images of the microstructure in samples: a,c) M1-ECAP4; and b,d) M2-ECAP4.

After significant additional atomic intermixing by HPT (Figure 6), the formation of phases was expected in the outer regions ($r > 0.3\ R$) of samples M1-ECAP1-HPT and M2-ECAP1-HPT. Bright field (BF) and dark field (DF) TEM images shed light on such a possibility for samples M1-ECAP1-HPT (**Figure 9**a–c) and M2-ECAP1-HPT (**Figure 10**a–c). For both samples, the microstructures consisted of nanocrystalline grains with boundaries that were not well defined, as is typical for HPT-processed materials.[24,30,31] Furthermore, the formation of nanocrystalline microstructures was confirmed by the selected-area-electron-diffraction (SAED) patterns (inserts in Figure 9a and 10a). Although the grain boundaries were not well defined, an analysis of the DF and STEM images in Figure 9 and 10 gave an approximate grain size following ECAP + HPT of 50 nm for both materials.

TEM-EDS analysis confirmed that a uniform nearly-equiatomic composition (previously discussed in Section 3.1) was indeed reached in the outer regions of samples M1-ECAP1-HPT and M2-ECAP1-HPT, as illustrated by the elemental maps in Figure 9d and 10d.

3.3. Annealing Effect on Microstructure

Figure 11 shows STEM BF images of M1-ECAP4 and M2-ECAP4 samples after annealing at 500 °C for 1 h. In general, the microstructures are very similar to those before heat treatment (see Figure 7 for comparison), with minor grain growth, especially in the Ti region, where grains reached sizes of up to 1.5 μm. Further EDS analysis confirmed that the annealing treatment marginally increased the diffusion distance of elements, but this was not sufficient to form new phases.

The microstructure of HPT samples at the outer region ($r > 0.3\ R$) after the annealing treatment is presented in **Figure 12**a and **13**a together with the corresponding SAED patterns. It is evident that after heat treatment, the grain boundaries became clearer due to the extended recovery that occurred at higher temperatures, leading to the formation of high-angle grain boundaries. Notably, there is no significant grain growth observed in the microstructure of both M1 and M2 compositions. This suggests that the elements in the solid solution restrict grain boundary movement, minimizing grain growth.

EDS elemental maps in Figure 12b and **13**b confirms slight segregation during the annealing treatment. This phenomenon results in the formation of new phases in the material. Previous studies have reported the formation of a ZrHf-rich phase with an HCP structure and a TaNb-rich phase with a BCC structure after an annealing treatment.[11,13,14,30,31]
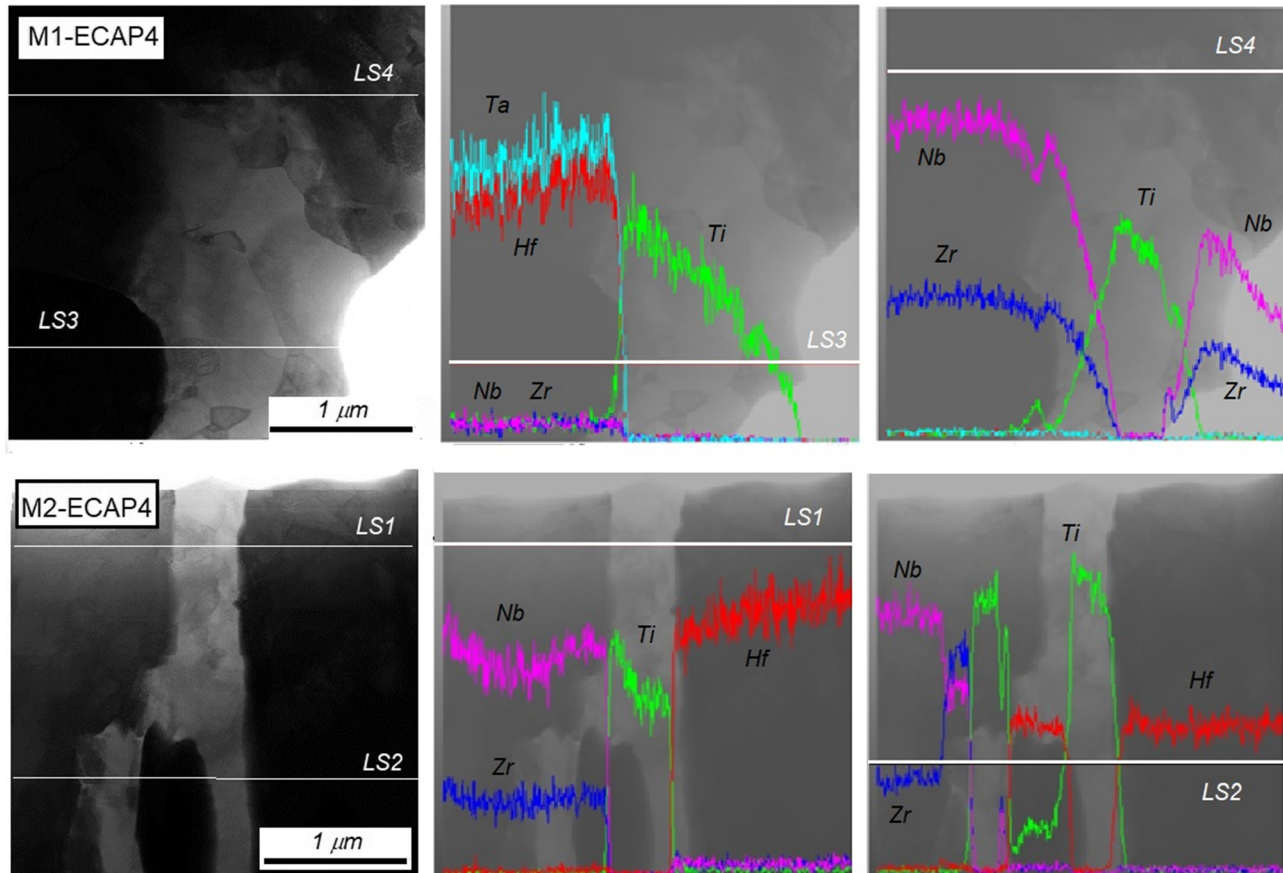
Figure 8. Example line-scan profiles across the particle boundaries in samples M1-ECAP4 and M2-ECAP4.

Table 4. Mean value of the diffusion distance d (nm) and standard deviation Std (nm).

	Ti/Hf	Ti/Zr	Hf/Zr	Nb/Ti	Nb/Zr	Hf/Nb	Ta/Ti	Ta/Nb	Ta/Zr
M1-ECAP4: d	50	134	59	186	103	100	126	83	42
M1-ECAP4: Std	12	71	18	145	52	24	53	56	9
M2-ECAP4: d	94	122	127	69	111	–	–	–	–
M2-ECAP4: Std	51	53	43	25	48	–	–	–	–

3.4. XRD Analysis of Phases

Results of XRD analysis are summarized in **Figure 14**, **15**, and **16**. After four ECAP passes, all diffraction peaks could be indexed and attributed to different constituents of the BE powder mixtures (Figure 14). Furthermore, a BCC ZrNb phase with a lattice parameter of $a = 3.47$ Å was discovered in both alloys. Considering its very small volume fraction (0.1%) and the disappearance of its peak (at $2\theta \approx 54°$) after annealing (Figure 15), a hypothesis emerged that BCC ZrNb phase observed after four ECAP passes forms likely within an interfacial zone between Zr and Nb particles. This hypothesis is consistent with the discussion in Section 3.2 regarding the width of the diffusion distance.

After the additional large strain imposed by HPT, the formation of two, more-consequential, newly formed phases was discovered in both the central and outer regions of the samples (Figure 16 and **Table 5**), with their parameters and volume fraction defined by the Rietveld refinement method. For alloy M1, the larger volume fraction (75–86%) comprised the BCC Nb-rich phase with space group Im–3 m, and the smaller volume fraction (14–25%) was the HCP Hf-rich phase with space group P63/mmc (Table 5). Similarly, for the M2-alloy, the larger volume fraction (82–84%) and smaller volume (16–18%) constituted the same two phases, respectively (Table 5).

The two-phase structures developed during SPD of BE powders in the present work contrasted to those found for both TiZrNbHfTa and TiZrNbHf alloys synthesized by arc melting.
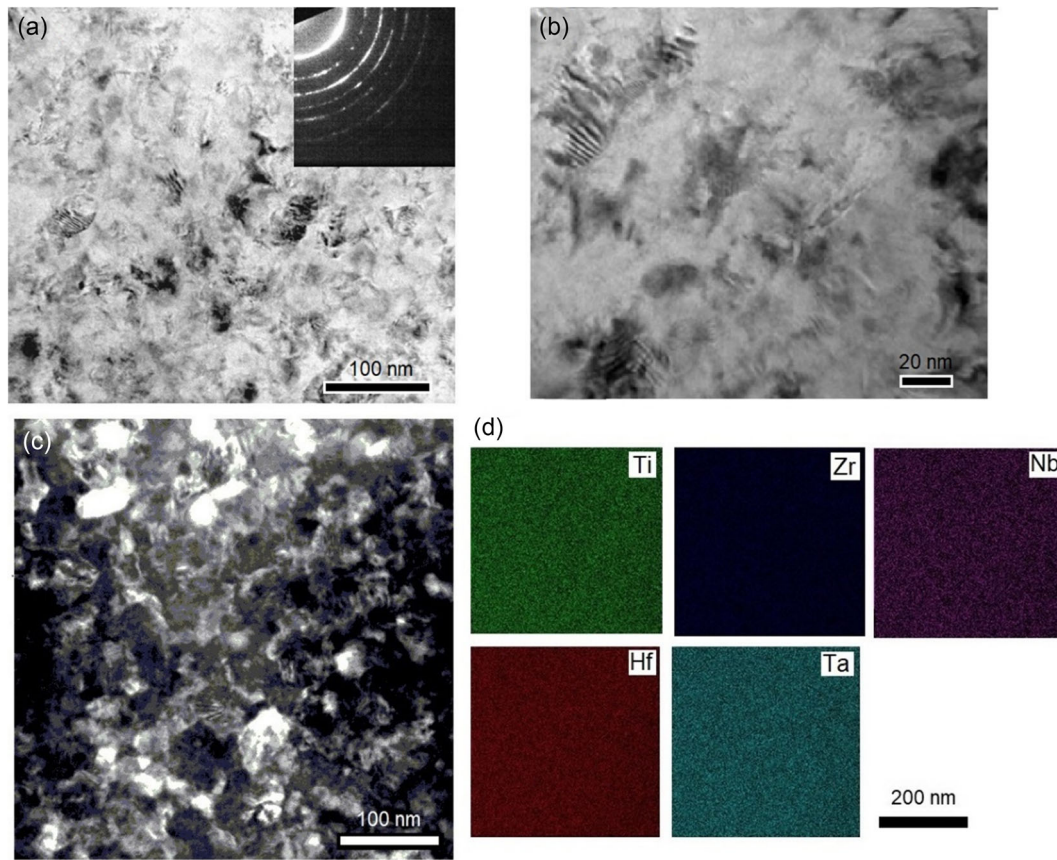
Figure 9. Microstructure of sample M1-ECAP1-HPT: a) BF TEM image with electron diffraction pattern; b) BF TEM image at higher magnification; c) DF TEM image; and d) corresponding EDS elemental maps.

Specifically, in the as-cast state and as well as after annealing at high temperatures (above 1000 °C), the former materials typically exhibit a single-phase (BCC) solid solution.[11,30,31] It has also been found that both TiZrNbHfTa and TiZrNbHf produced via melt synthesis maintain their BCC single-phase structures during subsequent HPT processing.[30,31] The corresponding lattice constant for melt-synthesized TiZrNbHfTa was 3.411 Å,[29] while that for TiZrNbHf was 3.438 Å.[30] These values are slightly higher than those for the BCC phase developed in samples of powder-synthesized M1-ECAP1-HPT and M2-ECAP1-HPT in the present work (Table 5).

After annealing of M1-ECAP1-HPT and M2-ECAP1-HPT for 1 h at 50 °C, new peaks were visible in the XRD profiles (Figure 16). In this regard, it has been found previously[30] that any heat treatment of nanocrystalline TiZrNbHfTa (M1) below 1000 °C results in the decomposition of the BCC phase. In addition, the specific type of lattice and its parameters depend on temperature and annealing time. In the present work, HPT-processed TiZrNbHfTa (M1) having a BCC structure with a lattice parameter of 3.411 Å decomposed during annealing for one hour at 500 °C into two phases, NbTa-rich BCC with $a = 3.355$ Å and ZrHf-rich HCP with $a = 3.198$ Å and $c = 5.067$ Å; while TiZrNbHf alloy (M2) decomposed in the three phases two BCC ($a = 3.391$ Å and $a = 3.324$ Å) and one HCP ($a = 3.195$ Å and $c = 5.085$ Å).

For comparison, in ref. [32] an annealing up to a temperature of 467 °C resulted in decomposition of the single-phase BCC TiZrNbHf alloy (M2) into two BCC structures with lower ($\approx$0.3427 nm) and higher ($\approx$0.3485 nm) lattice constants compared to the initial state ($\approx$0.3438 nm). Heat treatment between 467 and 617 °C resulted in the nucleation of a Zr/Hf-rich HCP phase with a low volume fraction of the order of $\approx$5%. At 617 °C, the major BCC phase had two components with slightly different lattice constants. These two components were Zr/Hf rich and Nb-rich BCC structures with higher and lower lattice parameters, respectively.

3.5. SAED Pattern Analysis

The SAED patterns were also analyzed to determine the phases in the materials by calculating the angular-integrated intensity over the entire pattern, **Figure 17**. Figure 17a displays the integrated intensity versus scattering vector, for SAED patterns shown in Figure 9a and 10a. It was confirmed that all the concentric rings belonged to a high-entropy BCC phase. However, the existence of a "shoulder" at the left side of the first maximum could be attributed to an HCP structure. This finding is consistent with the XRD results, despite the fact that other reflections of the HCP phase were hidden behind the broad peaks of the BCC
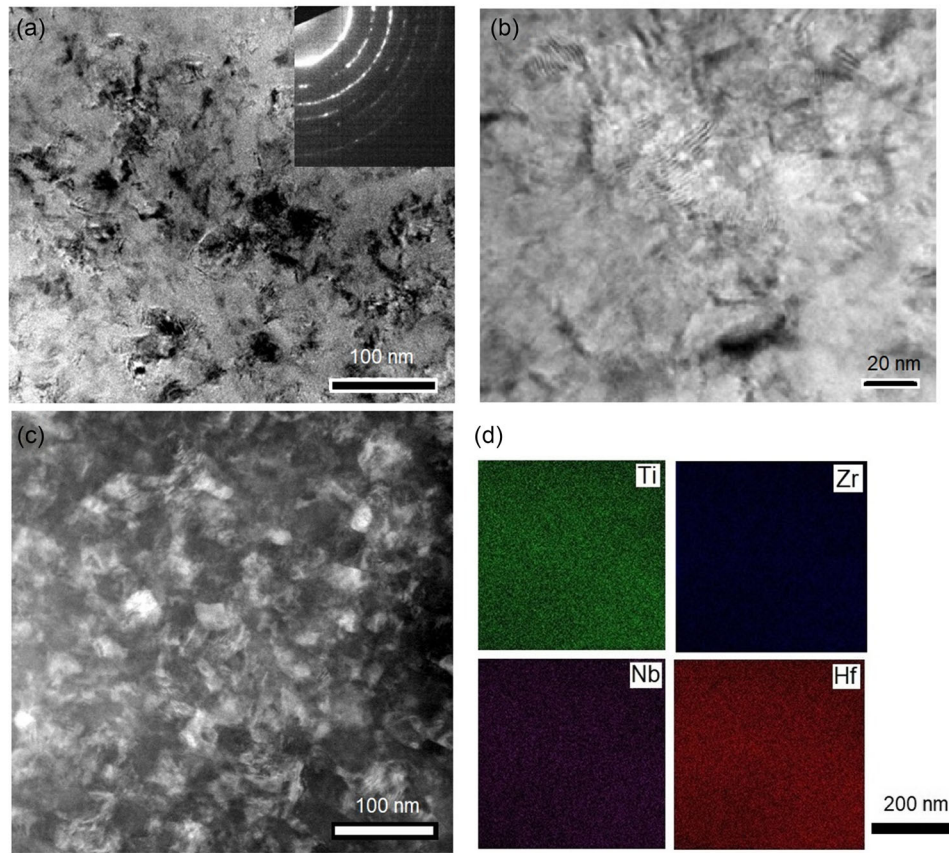
Figure 10. Microstructure of sample M2-ECAP1-HPT: a) BF TEM image with electron diffraction pattern; b) BF TEM image at higher magnification; c) DF TEM image; and d) corresponding EDS elemental maps.
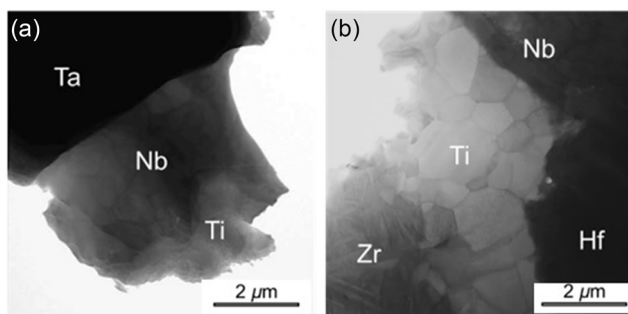

Figure 11. STEM BF images: a) M1-ECAP4-An; and b) M2-ECAP4-An.

solid solution and could not be revealed due to the poorer resolution of this method compared to XRD.

After calculating the d-spacing for different planes, the lattice parameters were estimated by the Pawley refinement method to be $a = 3.467$ Å and 3.590 Å for M1-ECAP1-HPT and M2-ECAP1-HPT, respectively. These lattice parameters were slightly higher than those in the literature. For example, lattice parameters equal to 3.411 Å (TiNbZrHfTa[30]) and 3.438 Å (TiNbZrHf[31]) have been reported for high entropy alloys made by arc melting followed by HPT. This difference may be attributed to completely different manufacturing route of M1 and M2 alloys. Moreover, it

is also worth noting that the SAED diffraction pattern is a site-specific measurement, and, thus, may vary slightly from one location to another with minor variations in chemical composition in the present samples.

Figure 17b displays the integrated intensity versus scattering vector, which was calculated from the SAED patterns shown in Figure 12a and 13a. It is evident that a hexagonal close-packed (HCP) structure formed during the annealing treatment in both compositions. The presence of the HCP structure is more pronounced in the M1 sample, as it exhibits multiple HCP peaks in the pattern. However, in the M2 graph, only the first and strongest HCP peak is visible, positioned to the left of the first BCC phase peak (110).

To accurately determine the peak positions of the HCP and BCC phases, the peaks were deconvoluted using the Origin software (9.9.5.167) with a pseudo-Voigt function. After calculating the d-spacing for different planes, the lattice parameters were estimated using the Pawley refinement method. For the BCC phase in the M1 sample, the lattice parameter was found to be $a = 3.420$ Å while for the HCP phase, a parameter was determined to be 3.240 Å, and c parameter was estimated as 5.294 Å.

In **Figure 18**, the TEM bright-field (BF) image of the M1-ECAP1-HPT-An sample is presented, along with the corresponding convergent beam electron diffraction (CBED) pattern of the grain marked in Figure 18a. a diffraction pattern with the unit
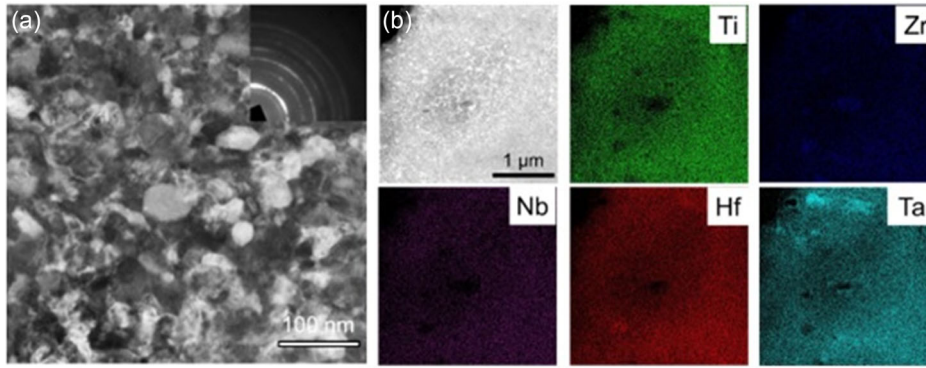
ADVANCED
SCIENCE NEWS

www.advancedsciencenews.com

ADVANCED
ENGINEERING
MATERIALS

www.aem-journal.com

Figure 12. M1-ECAP1-HPT-An sample: a) STEM DF image with its corresponding SAED pattern in the insert; b) EDS elemental maps.
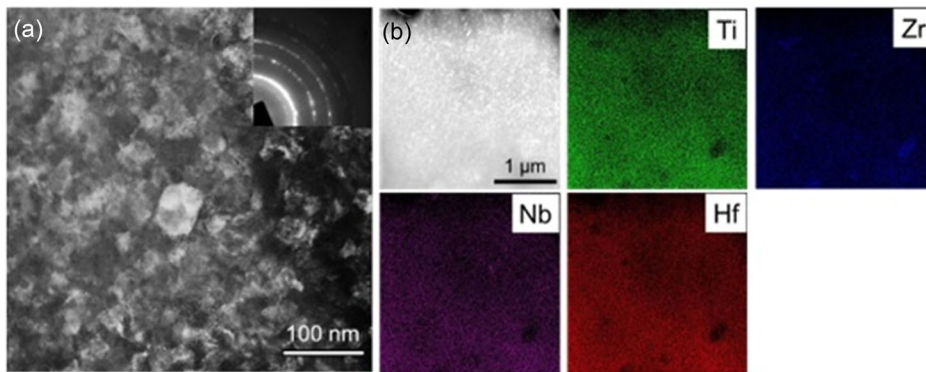

Figure 13. M2-ECAP1-HPT-An sample: a) STEM DF image with its corresponding SAED pattern in the insert b) EDS elemental maps.
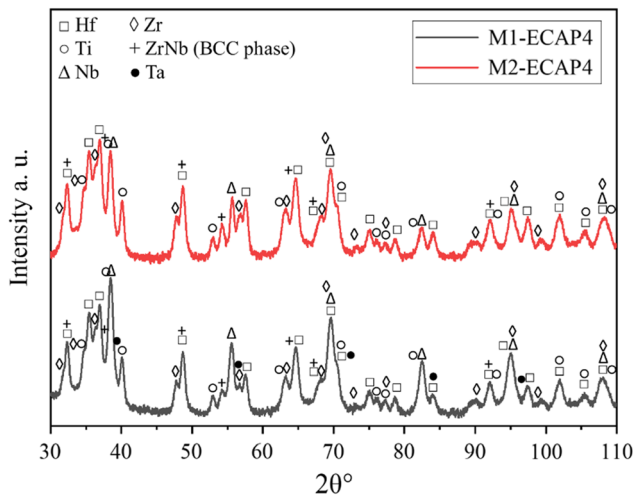

Figure 14. XRD profiles (on logarithmic scale) collected from samples M1-ECAP4 and M2-ECAP4 in the angular range $2\theta = 30°–110°$.
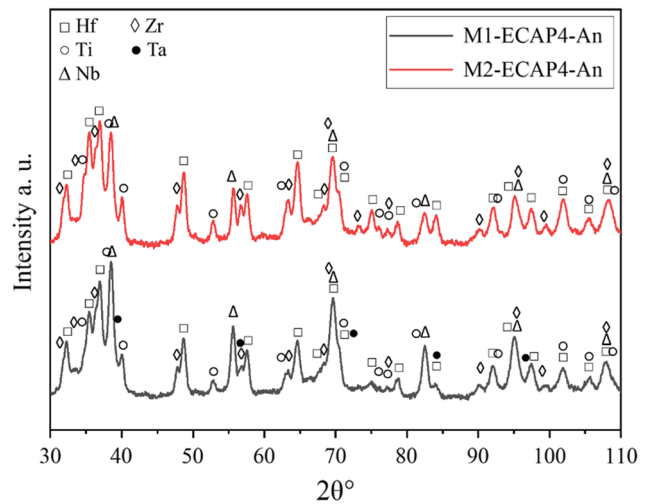

Figure 15. XRD profiles (on logarithmic scale) collected from samples M1-ECAP4-An and M2-ECAP4-An in the angular range $2\theta = 30°–110°$.

2301949 (12 of 15)

**ADVANCED
SCIENCE NEWS**

www.advancedsciencenews.com

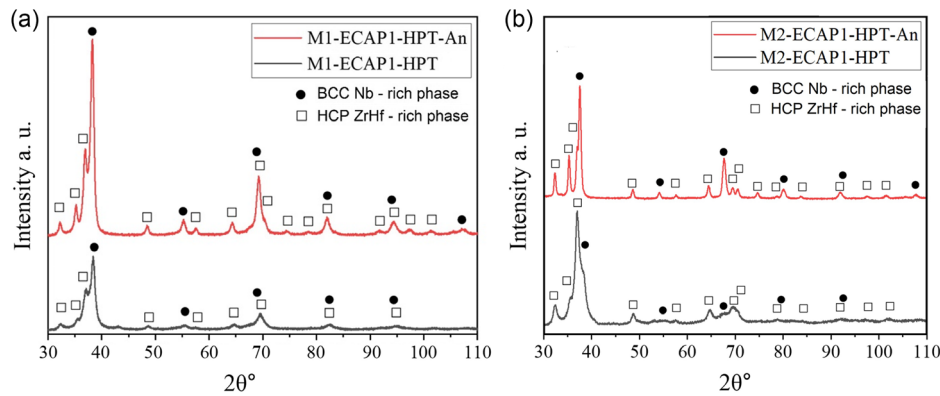**ADVANCED
ENGINEERING
MATERIALS**

www.aem-journal.com

Figure 16. XRD profiles (on logarithmic scale) collected from samples subjected to HPT before and after annealing in the angular range $2\theta = 30°$ to 110°: a) M1-ECAP1-HPT and M1-ECAP1-HPT-An; b) M2-ECAP1-HPT and M2-ECAP1-HPT-An.

Table 5. Lattice parameters and volume fractions of phases in samples subjected to HPT before and after annealing.

M1-ECAP1-HPT	Centre		Mid-radius		Edge	
	Cell [Å]	vol%	Cell [Å]	vol%	Cell [Å]	vol%
Im-3 m	3.310	75	3.302	79	3.309	86
P63/mmc	3.199	25	3.204	21	3.213	14
	5.065		5.071		5.067	
M2-ECAP1-HPT						
Im-3 m	3.298	82	3.397	87	3.383	84
P63/mmc	3.192	18	3.201	13	3.206	16
	5.046		5.073		5.072	
M1-ECAP1-HPT-An						
Im-3 m	3.303	69	3.312	73	3.3417	81
P63/mmc	3.193	31	3.193	27	3.224	19
	5.079		5.086		5.120	
M2-ECAP1-HPT-An						
Im-3 m	3.388	45	3.391	60	3.391	81
P63/mmc	3.195	36	3.195	27	3.199	19
	5.078		5.085		5.091	
Im-3 m_1	3.305	19	3.324	13	–	–

reflections along $g = 100$ (or $10\overline{1}1$ in Bravais–Miller notations) and $g = 1\overline{1}1$ (or $1\overline{1}01$) is clearly visible. Based on the measurement of the corresponding scattering vectors, we can determine the cell parameters as $a \approx 3.23$ A and $c \approx 5.34$ A. The grain has a [011] zone axis. Further EDS analysis reveals a higher concentration of Zr and Hf in this grain after heat treatment, Figure 18. Therefore, it can be concluded that the HCP phase formed during the annealing treatment corresponds to the ZrHf-rich phase as indicated in previous studies.[11,30]

It is worth noting that in both compositions, the lattice parameters of the high-entropy BCC phases are somewhat smaller than for pure components, indicating changes in the composition of these phases due to the annealing treatment. Additionally, the lattice parameters estimated from XRD measurements are slightly smaller than the lattice parameters calculated from SAED patterns, which is attributed to the residual chemical inhomogeneity of the mixture and the site-specific measurements of SAED pattern analysis.
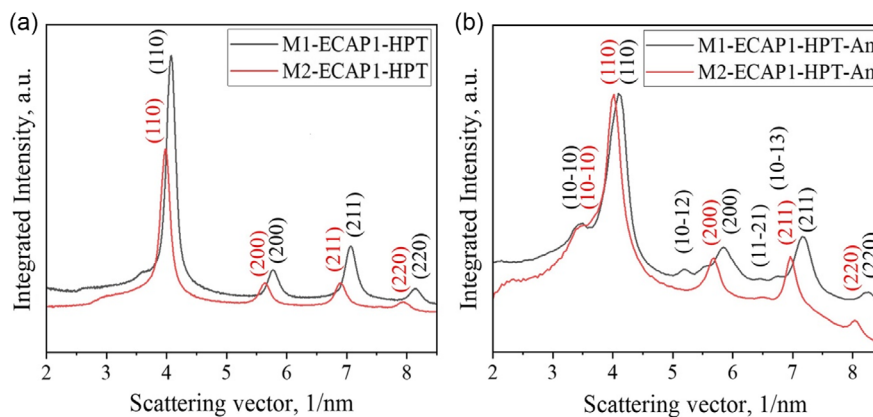
Figure 17. Integrated intensity versus scattering vector calculated from SAED patterns for samples: a) M1-ECAP1-HPT and M2-ECAP1-HPT; b) M1-ECAP1-HPT-An and M2-ECAP1-HPT-An.
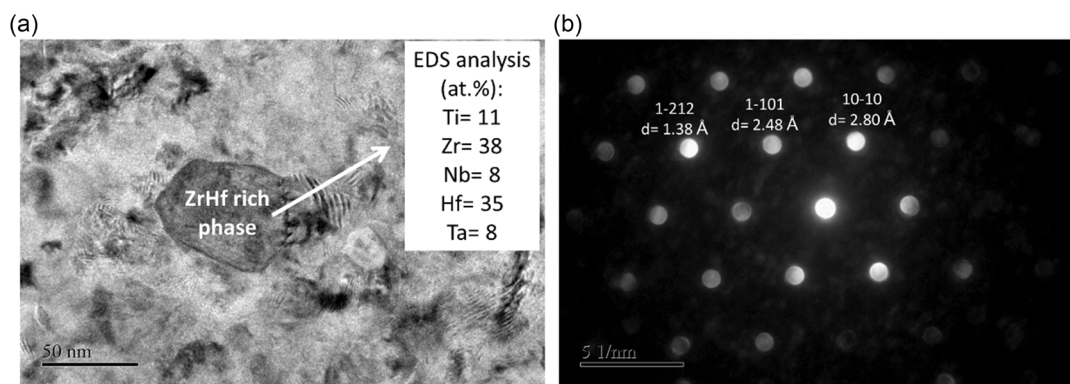

Figure 18. M2-ECAP1-HPT-An sample: a) TEM BF of; and b) the corresponding CBED pattern of the ZrHf-rich phase with HCP structure taken from the grain marked in (a).

4. Summary and Conclusions

A comparative investigation of two fundamentally different approaches for the synthesis, microstructure evolution, and mechanical properties of the RHEA HfNbTaTiZr and HfNbTiZr was performed. The two methods comprised conventional arc (button) melting, and a powder route based on mechanical alloying and consolidation via SPD.

Refractory high entropy alloys were synthesized from a blend of elemental powders using SPD methods. Two powder mixtures with the equiatomic compositions HfNbTaTiZr and HfNbTiZr were subjected to different levels of strain via equal-channel angular pressing (ECAP) and HPT.

It was found that atomic intermixing commences in ECAP when the accumulated effective strain reaches 4.6, and a turbulent flow pattern is established. A homogeneous atomic mixture is obtained using subsequent HPT, which is better suited for creating a turbulent flow pattern, to a strain level of $\approx$40 in the outer region of samples ($r > 0.3\ R$). In particular, an ultrafine-grain microstructure with a grain size below $\approx$50 nm is thus created here.

Four ECAP passes at 50 °C does not result in the formation of a typical RHEA BCC phase despite the presence of interfacial zones between particles and defect-driven (pipe) diffusion. Nevertheless, a single ECAP pass is sufficient to create a bulk sample suitable for subsequent HPT processing.

After ten HPT revolutions at room temperature, both alloys in the outer region of the disc undergo the formation of new phases differing from those observed when RHEA are obtained by a molten route. In the case of HfNbTaTiZr, the HPT leads to a predominant constituent (volume fraction = 75–86%) consisting of a Nb-rich BCC phase and a smaller volume fraction (14–25%) comprising a ZrHf-rich HCP phase. For HfNbTiZr, the principal phase (82–84%) constitutes a Nb-rich BCC phase; a smaller volume fraction (16%–18%) consists of a ZrHf-rich HCP phase. After annealing treatment, the volume fraction of BCC phase decreased on average to 75% and volume fraction of HCP phase increased to $\approx$25% in both alloys. Notably as result of annealing, the BCC phase in M2 alloy was transformed into two BCC phases with different cell parameters.

Vickers microhardness measurements demonstrated an increase in strength with the accumulation of effective strain above 40 and its saturation. These results are consistent with the published data for similar alloys synthesized by arc melting followed either by rolling or SPD, or by powder consolidation based on sintering and SPD. After short annealing the

Vickers hardness increased significantly for all samples and this phenomenon is analyzed.

Conflict of Interest

The authors declare no conflict of interest.

Data Availability Statement

The data that support the findings of this study are available from the corresponding author upon reasonable request.

[1] D. B. Miracle, O. N. Senkov, *Acta Mater.* **2017**, *122*, 448.

[2] X. Ren, Y. Li, Y. Qi, B. Wang, *Materials* **2022**, *15*, 2931.

[3] C. C. Koch, *J. Mater. Res.* **2017**, *32*, 3435.

[4] V. H. Hammond, M. A. Atwater, K. A. Darling, H. Q. Nquyen, L. J. Kecskes, *JOM* **2014**, *66*, 2021.

[5] V. Segal, *Materials* **2018**, *11*, 1175.

[6] C. Haase, R. Lapovok, H. P. Ng, Y. Estrin, *Mater. Sci. Eng.* **2012**, *A550*, 263.

[7] C. Bettles, M. Moss, R. Lapovok, *Mater. Sci. Eng.* **2009**, *A515*, 26.

[8] S. Divinski, G. Wilde, *Mater. Sci. Forum* **2008**, *584-586*, 1012.

[9] O. N. Senkov, S. L. Semiatin, *J. Alloys Compd.* **2015**, *649*, 1110.

[10] O. N. Senkov, A. L. Pilchak, S. L. Semiatin, *Metall. Mater. Trans.* **2018**, *49A*, 2876.

[11] S. Y. Chen, Y. Tonga, K.-K. Tseng, J.-W. Yeh, J. D. Poplawsky, J. G. Wen, M. C. Gao, G. Kim, W. Chen, Y. Ren, R. Feng, W. D. Li, P. K. Liaw, *Scr. Mater.* **2019**, *158*, 50.

[12] C.-H. Tu, Y.-C. Lai, S.-K. Wu, Y.-H. Lin, *Mater. Lett.* **2021**, *303*, 130526.

[13] H. Huang, Y. Sun, P. Cao, Y. Wu, X. Liu, S. Jiang, H. Wang, Z. Lu, *Scr. Mater.* **2022**, *211*, 114506.

[14] P. T. Hunga, M. Kawasaki, J.-K. Hanb, J. L. Lábára, J. Gubiczaa, *Mater. Character.* **2020**, *168*, 110550.

[15] J. Málek, J. Zýka, F. Luká, M. Vilémová, T. Vlasák, J. Cížek, O. Melikhova, A. Macháčková, H.-S. Kim, *Materials* **2019**, *12*, 4022.

[16] J. Málek, J. Zýka, F. Luká, J. Cížek, L. Kuncická, R. Kocich, *Metals* **2019**, *9*, 1324.

[17] F. Lukác, M. Vilémová, M. Klementová, P. Minárik, T. Chráska, *Mater. Lett.* **2021**, *286*, 129224.

[18] R. Kulagin, Y. Beygelzimer, Y. Ivanesenko, A. Mazilkin, H. Hahn, *IOP Conf. Ser.: Mater. Sci. Eng.* **2017**, *194*, 012045.

[19] O. Senkov, D. B. Miracle, K. J. Chaput, J.-P. Couzinie, *J. Mater. Res.* **2018**, *33*, 3092.

[20] S. Gorsse, J.-P. Couzinie, *C. R. Phys.* **2018**, *19*, 721.

[21] R. Lapovok, D. Tomus, B. C. Muddle, *Mater. Sci. Eng.* **2008**, *A490*, 171.

[22] R. Lapovok, D. Tomus, C. Bettles, *Scr. Mater.* **2008**, *58*, 898.

[23] Y. Beygelzimer, Y. Estrin, A. Mazilkin, T. Scherer, B. Baretzky, H. Hahn, R. Kulagin, *J. Alloys Compd.* **2021**, *878*, 160419.

[24] J. Cízek, P. Hausild, M. Cieslar, O. Melikhova, T. Vlasak, M. Janecek, R. Kral, P. Harcuba, F. Lukac, J. Zýka, J. Malek, J. Moon, H. S. Kim, *J. Alloys Compd.* **2018**, *768*, 924.

[25] O. Renk, A. Hohenwarter, B. Schuh, J. H. Li, R. Pippan, in *36th Risø Int. Symp. on Materials Science IOP Publishing, IOP Conf. Series: Materials Science and Engineering*, Vol. 89, Risø, Denmark, September 2015, p. 012043.

[26] P. Cengeri, M. B. Kerber, E. Schafler, M. J. Zehetbauer, D. Setman, *Mater. Sci. Eng. A* **2019**, *742*, 124.

[27] A. Medvedev, M. Murashkin, N. Enikeev, R. Z. Valiev, P. D. Hodgson, R. Lapovok, *Adv. Eng. Mater.* **2018**, *20*, 1700867.

[28] Y. Estrin, A. Molotnikov, C. H. J. Davies, R. Lapovok, *J. Mech. Phys. Solids* **2008**, *56*, 1186.

[29] (Eds: T.B. Massalski, H. Okamoto, P.R. Subramanian, L. Kacprzak), *Binary Alloy Phase Diagrams* 2nd ed., ASM International, Almere, The Netherlands **1990**.

[30] B. Schuh, B. Volker, J. Todt, N. Schell, L. Perriere, J. Li, J. P. Couzine, A. Hohenwarter, *Acta Mater.* **2018**, *142*, 201.

[31] P. T. Hung, M. Kawasaki, J.-K. Han, J. L. Gubicza, *Mater. Character.* **2020**, *168*, 110550.

[32] P. P. Cao, H. L. Huang, S. H. Jiang, X. J. Liu, H. Wang, Y. Wu, Z. P. Lu, *J. Mater. Sci. Technol.* **2022**, *122*, 243.